Microvascular Thermal Equilibration in Rat Cremaster Muscle

LIANG ZHU,* DANIEL E. LEMONS,† and SHELDON WEINBAUM*

*Department of Mechanical Engineering and †Department of Biology, City College of The City University of New York,
New York, NY

Abstract—A new experimental approach was developed to obtain the first direct measurements of the axial countercurrent thermal equilibration in a microvascular tissue preparation using high resolution infrared thermography. Detailed surface temperature measurements were obtained for an exteriorized rat cremaster muscle in which pharmacological vasoactive agents were used to change the local blood flow Peclet number from 1 to 14 in the feeding artery. Under normal conditions, only the 1A arteries (>70 μm diameter) showed thermal nonequilibration with the surrounding tissue. The theoretical model developed by Zhu and Weinbaum (28) for a two-dimensional tissue preparation with arbitrarily embedded countercurrent vessels was modified to include axial conduction and the presence of the supporting glass slide. This modified model was used to interpret the experimental results and to relate the surface temperature profiles to the bulk temperature profiles in the countercurrent artery and vein and the local average tissue temperature in the cross-sectional plane. Surface temperature profiles transverse to the vessel axis are shown to depend significantly on the tissue inlet temperature. The eigenfunction for the axial thermal equilibration depends primarily on the blood flow Peclet number and the environmental convective coefficient. The theoretical results predict that when ρ_{ar}*Pe is less than 1 mm (the range in our experiments), axial conduction is the dominant mode of axial thermal equilibration. For $1 < \rho_{ar}$*Pe < 3 mm, countercurrent blood flow becomes comparable to axial conduction, whereas, when ρ_{ar}*Pe > 3 mm, countercurrent blood flow is the dominant mode of axial thermal equilibration. Therefore, for ρ_{ar}*Pe > 3 mm the axial equilibration length is proportional to the blood flow Peclet number, as predicted previously by Zhu and Weinbaum in a study in which axial conduction was neglected. It also is shown that the axial decay of the tissue temperature at low perfusion rates can be described by a simple one-dimensional Weinbaum-Jiji equation with a newly derived conduction shape factor

Keywords—Thermal equilibration length, Microvascular heat transfer, Rat cremaster muscle, Infrared thermography, Countercurrent heat exchange.

INTRODUCTION

It is widely known that blood flow distribution and detailed microvascular geometry have a profound effect on the heat exchange between the blood and tissue and the heat exchange of the tissue near the surface of the body with the environment. Most investigations of countercurrent heat exchange in humans and mammals before 1980 examined the heat transfer between the large countercurrent arteries and veins in the limbs (7,16,17,19). No equivalent experiments have been performed successfully in microvascular tissue preparations. These experiments require high spatial resolution temperature measurements on a length scale of the diameter of the microvessels. This study, to the best of our knowledge, presents the first measurements of countercurrent axial thermal equilibration in the microcirculation.

The first quantitative relationship to describe heat transfer in living tissue was proposed by Pennes (17). Pennes's equation assumed a uniform perfusion source term that was thought to describe blood-tissue heat transfer occurring in the capillary beds. This fundamental assumption has been questioned by several investigators since 1980, when Chen and Holmes (10) first showed, by using simple theoretical models, that blood-tissue thermal equilibration occurred in 50- to 500-μm-diameter vessels and not in capillary beds. Later, models derived by Weinbaum *et al.* (23) showed that the primary mechanism by which the microvascular blood flow altered the tissue heat transfer was incomplete countercurrent exchange in these thermally significant microvessels. A new bioheat transfer equation, which combined the convective effect of countercurrent pairs and capillary bleed-off from these vessels with the traditional conduction term and showed that these effects could be represented as an enhancement in thermal conductivity, k_{eff}, was derived by Weinbaum and Jiji (21).

Motivated by these theoretical studies, several *in vivo* and *in vitro* experiments have been performed to elucidate how and where microvascular heat transfer occurs. In experiments performed by Weinbaum *et al.* (23), thermocouple traverses across a rabbit thigh were performed *in vivo* to show the importance of countercurrent heat exchange. The arterial temperature was found to be nearly
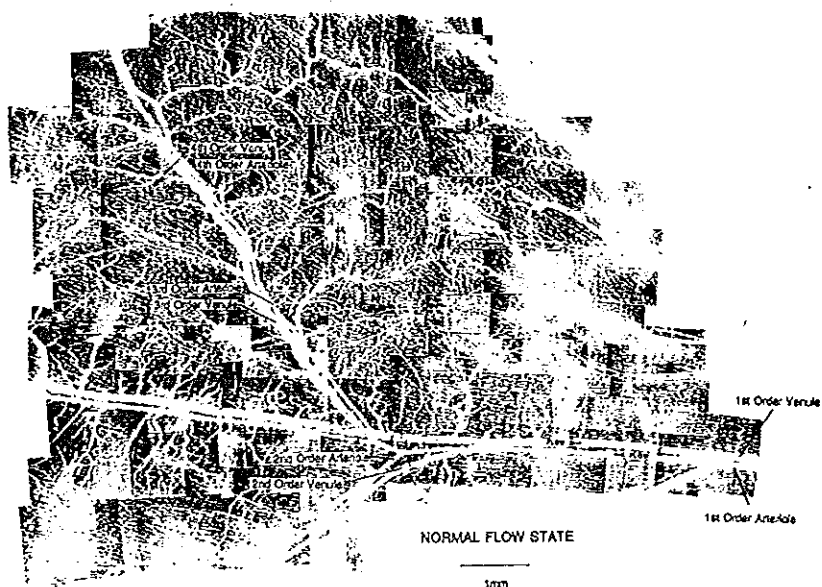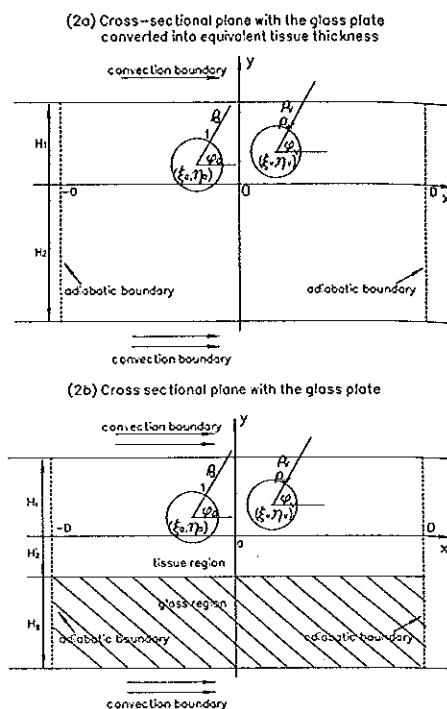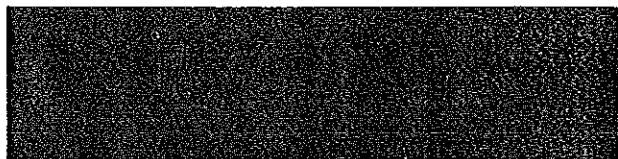
NORMAL FLOW STATE

1mm

(2a) Cross-sectional plane with the glass plate converted into equivalent tissue thickness

(2b) Cross sectional plane with the glass plate

FIGURE 1. Photomontage of the rat cremaster preparation provided by Dr. H. H. Liposwky. ↑

FIGURE 2. Schematic of the cross-sectional plane with and without the glass plate. →

Recirculating Cremaster Tissue Bath

Top View of Bath

Side View

FIGURE 3. Schematic of the experimental setup used to study the rat cremaster muscle. ↑

FIGURE 4. Thermal images of the cremaster muscle at four different levels of the Peclet number of the main 1A arteriole. The spectrum at the bottom shows the relationship of image color to temperature. The right side of each image is the proximal edge of the muscle. →

Low Flow (Pe=2.8)

Intermediate Flow (Pe=4.8)

Moderate flow (Pe=9.2)

High Flow (Pe=14)

26.6 °C   27.7 °C   29.7 °C
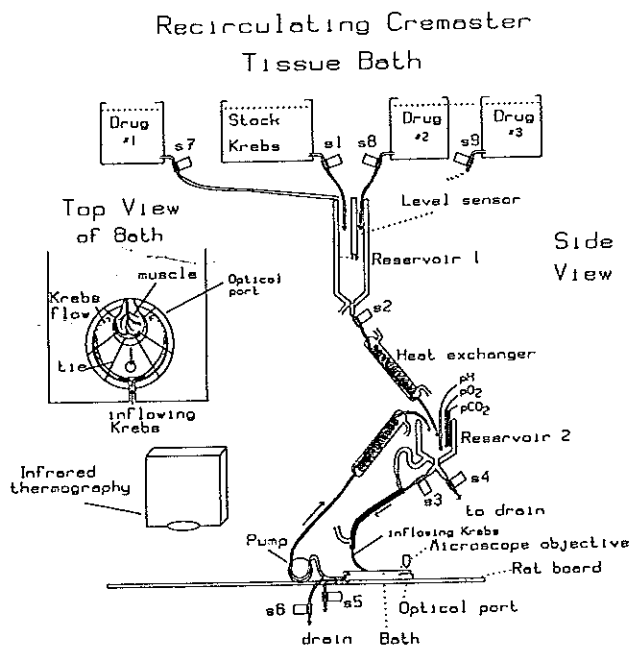
equal to the venous temperature for any countercurrent pair encountered along the traverse. Subsequently, Lemons et al. (15) obtained detailed temperature profiles, which strongly supported the premise in the Weinbaum-Jiji equation that thermal equilibration occurred in the larger countercurrent microvessels. High resolution temperature measurements in the vicinity of numerous vessels of 50–500 μm diameter, were reported for a rabbit thigh. The results showed that the microvascular artery-vein temperature differences in these primary heat exchange vessels were only of the order of 0.1–0.2°C for vessels 100 μm in diameter or larger, whereas for vessels smaller than 100 μm in diameter, there were no measurable temperature disturbances. Crezee and Lagendijk (11) inserted a small plastic tube into the tissue of a bovine kidney and measured the disturbance temperature fields in a plane perpendicular to the tube while heated water was circulated through it, and the kidney cortex was perfused at different rates. These investigators also used thermocouples to map the temperature distribution in the tissue of isolated perfused bovine tongues at various perfusion rates (12). The temperature measurements in these experiments were found to agree better with a perfusion enhanced k_{eff} as opposed to the perfusion source term in the Pennes equation. Roemer et al. (18) measured steady-state temperature profiles in canine thighs heated by scanned focused ultrasound. A comparison was made with both Pennes and Weinbaum-Jiji models, and a better qualitative agreement was found with the former. Several investigators (1,26) have attempted to relate the measured tissue temperature profiles or the effective conductivity of a perfused kidney cortex to the local microvascular geometry and flow and the predictions of the Pennes and the Weinbaum-Jiji bioheat equations. Anatomical studies, however, have shown that this is a poor model for muscle tissue because the interlobular arteries and veins do not occur as closely spaced artery-vein pairs. It is difficult to reconcile these different results because there was neither an experimental method for measuring the axial thermal equilibration in different-size microvessels in an in vivo tissue preparation nor an adequate theoretical model for relating this equilibration to the local blood perfusion.

Microvascular blood flow commonly is examined in a variety of two-dimensional tissue preparations. Rabbit ear, frog mesentery, rat cremaster muscle, and hamster check pouch are a few of the more widely used preparations. These preparations have been used extensively in the past in experiments to measure key parameters in microvascular beds (e.g., hematocrit distribution), in mass transfer studies using fluorescent tracers, in studies of vasoactive drugs, and in other applications. In this study, we used the rat cremaster muscle to study for the first time the axial thermal equilibration between blood and tissue in vivo. In a companion study (27), this tissue preparation

was used to study the temperature response of a microvascular bed to hyperthermia. As shown in Fig. 1, the rat cremaster muscle preparation has the important advantages of being nearly transparent and having uniform thickness. These features allow the accurate measurements of vessel number density, diameter, and blood flow in several successive generations of vessels. All 1A and 2A vessels and most 3A vessels in the preparation are present as countercurrent artery-vein pairs. Depending on rat age and size, the feeding arteriole (1A) varies from 50 to 200 μm in diameter. Previous theoretical studies suggested that vessels of this size are the most important in blood-tissue energy exchange.

High resolution infrared thermography is a noninvasive technique that can be used to measure the detailed in vivo surface temperature field above individual microvessels in a two-dimensional tissue preparation, such as that shown in Fig. 1. Therefore, a theoretical model is required to relate the surface temperatures that are measured in the experiment to the temperature of the blood in the vessels and the axial thermal equilibration that occurs between the tissue and the artery-vein pair beneath the surface. It is widely known that the equilibration length for a particular vessel pair varies with the blood flow Peclet number and, therefore, this length varies as the diameter and the flow velocity change during physiological regulation. Changes in caliber and flow rate of the feeding arterioles can be produced by pharmacologically vasoactive agents. It is, therefore, possible to experimentally examine the relationship between the thermal equilibration length and the blood flow Peclet number in the feeding 1A artery by introducing increasing concentrations of vasoactive drugs.

The boundary conditions for countercurrent vessels in a thin tissue preparation depart significantly from those of many previous studies that have considered either vessels embedded in an infinite or semi-infinite medium (6,13,20) or countercurrent heat transfer in a tissue cylinder of finite radius (4,24,25,29,30). The solutions for these flow configurations cannot be applied to the present flow geometry, and Zhu and Weinbaum (28) previously presented a simplified model for the two-dimensional tissue preparation, which is shown in Fig. 2a. The artery-vein pair is represented by two line sources that are positioned arbitrarily in the cross-sectional plane of the preparation. An analytic solution for a Green's function was then derived, which satisfied all the tissue boundary conditions for this flow geometry in the cross-sectional plane of the vessels. This solution was shown to be exact when the ratio of blood to tissue conductivity was $K' = 1$ and highly accurate when $K' \neq 1$. This initial model was used to design and test the feasibility of this study.

The initial model described above did not take into account the axial heat conduction in the tissue region or the effect of the glass plate on which the rat cremaster

muscle preparation was placed during the experiments. The experiments showed, however, that, at low blood flow rates, axial heat conduction is comparable to axial heat transfer as a result of the countercurrent flow in the blood vessels. A more realistic model, schematically shown in Fig. 2b, was, therefore, developed in this study to allow a more detailed comparison with experiments. This modified three-dimensional model considers both axial conduction and the effect of the supporting glass plate. The addition of axial conduction changes the nature of the boundary value problem and enables one to examine important new features, such as different artery and tissue entrance temperature, which could not be addressed when the model of Zhu and Weinbaum (28) was used.

METHODS

Experimental Methods

Fourteen male Sprague-Dawley rats (weight = mean $\pm$ SD, 153 $\pm$ 27 g) were used in this study. The animals were anesthetized with an intraperitoneal injection of sodium pentobarbital solution (40 mg/kg). Supplemental doses were administered as needed. A tracheal tube was inserted to maintain a patent airway. After anesthesia administration, the rat was placed on a water-jacketed pad to maintain a constant rectal temperature, which was monitored throughout the experiment with a thermocouple inserted into the rectum. The surgical procedure required approximately 30 min, and the subsequent experimental procedure required approximately 1 hr.

The left cremaster muscle was dissected from the scrotal skin and testicle for *in vivo* microvascular observation as described previously (2,14). This exteriorized cremaster muscle was extended into a flattened sheet and held with silk sutures over an optical window in a tissue bath at room temperature. The schematic diagram for the experimental setup is shown in Fig. 3. The tissue bathing solution was drawn from stock reservoir (reservoir 1) containing a modified Krebs-Ringer solution that consisted of 6.6 g/l NaCl, 0.35 g/l KCl, 0.28 g/l $MgSO_4$, 0.28 g/l $CaCl_2 \cdot 2H_2O$, 0.16 g/l KH_2PO_4, 2.09 g/l dextrose, and 2.14 g/l $NaHCO_3$ dissolved in filtrated water. The cremaster muscle is sensitive to PO_2, PCO_2, and pH, all of which were monitored by an Anafaze 8LS controller (Anafaze Measurement and Control, Watsonville, CA) that adjusted the bubbling rate of CO_2 and N_2 in the recirculating reservoir (reservoir 2) to maintain a PO_2 of 15–30 torr, a PCO_2 of 35–45 torr, and a pH of 7.4.

The preparation was transilluminated on the microscope stage (Zeiss, Thornwood, NY; ACM) and viewed through a 10X Nikon water immersion objective. During the experiment, the field of view was displayed on a closed circuit camera and videotaped for later analysis.

The average blood flow velocity, u, in the feeding arteriole was equal to the centerline blood velocity, V, divided by 1.6 (5). The blood flow Peclet number, Pe, is given by

$$Pe = 2\gamma_f C_f \rho_{ar}^* u/k_f$$

where γ_f is blood density, C_f is specific heat of blood, k_f is blood thermal conductivity, u is average blood flow velocity of the microvessel, and ρ_{ar}^* is vessel radius (in μm). Centerline red blood cell velocity was measured with an optical Doppler velocimeter (Microcirculation Research), and vessel radius was measured from the videotape with an electronic video caliper (Microcirculation Research). The preparation could be positioned either under the light microscope optics or rotated into place under a Hughes Probeye infrared camera (Hughes, Carlsbad, CA) to obtain a high resolution thermal image of the muscle. The infrared camera was positioned 10 cm to the left of the optical axis so that movement between the two measurement systems could occur rapidly, and a registration mark ensured reproducibly accurate placement of the muscle under the optical axis. The infrared camera had an auxiliary 5-mm lens that yielded an optical resolution of 125 μm and temperature resolution of 0.1°C. One calibrated copper-constantan thermocouple was used to measure the environmental temperature, and two other thermocouples were held in position beneath the muscle at separate locations to provide an absolute temperature reference for the infrared camera. The experiment was controlled by, and the data were acquired and recorded with LabView software (National Instruments, Austin, TX) running on a Macintosh computer.

Measurement Protocol

A 30-min stabilization period followed surgery to allow the preparation to achieve an initial steady-state blood flow. Then four trials were conducted in each experiment, one for each of four different microvascular blood flow rates. To induce changes in the blood flow Peclet numbers in a feeding arteriole, a vasoconstrictor, NE (10^{-5} M), or a vasodilator, sodium nitroprusside (10^{-7} M, 10^{-6} M, and 10^{-5} M), was added for each trial. After addition, a 10-min period was given for the preparation to reach equilibrium. After all parameters (temperature, velocity, and diameter) stabilized, the images of the feeding arteriole-venule pair and the centerline red blood cell velocity were recorded continuously for a 2-min measurement period. Then, within 30 sec, the preparation was rotated under the infrared camera, and the solution inside the tissue bath was drained. The thermal image of the preparation and the temperatures measured by thermocouples were recorded. A thin plastic wrap was placed on the muscle surface to prevent evaporation. Immediately after the thermal image

was completed, the rat was repositioned under the optical microscope, and the velocity and diameter were measured again to verify that they had remained unchanged while the thermal image was being obtained. Next, a new concentration of drug was added to obtain stepwise changes in blood flow and to reach a new equilibrium, and the above-described procedure was repeated until the sodium nitroprusside (10^{-5} M) trial was finished. Changes in vessel diameter, vessel center to center spacing, and flow velocity, therefore, could be recorded for each flow condition and used as input in the theoretical model.

Experimental Results

Figure 4 shows a sequence of high resolution infrared images of a single rat cremaster muscle at four different blood flow rates. Figure 5 shows the axial surface temperature profiles above the central arteriole of the cremaster muscle at four different blood flow rates. Increasing the blood flow rate produced a higher inlet temperature at the proximal boundary (on the left) at $z^* = 0$ mm and an elevation of the temperature of the entire preparation. The maximum point in the temperature profiles normal to the vessel axial direction was found to be a good indication of the location of the feeding arteriole. As observed in Fig. 4 the thermal disturbance caused by the blood vessels became more evident as the blood flow rate increased.

The horizontal surface temperature profiles normal to the axial direction of the 1A feeding artery-vein pair are shown in Fig. 11. These profiles revealed the somewhat surprising fact that this temperature field was almost uniform in the lateral direction. The comparison between experimental data and theoretical predictions presented below explains this unexpected observation and interprets the results shown in Figs. 4, 5, 10, and 11.
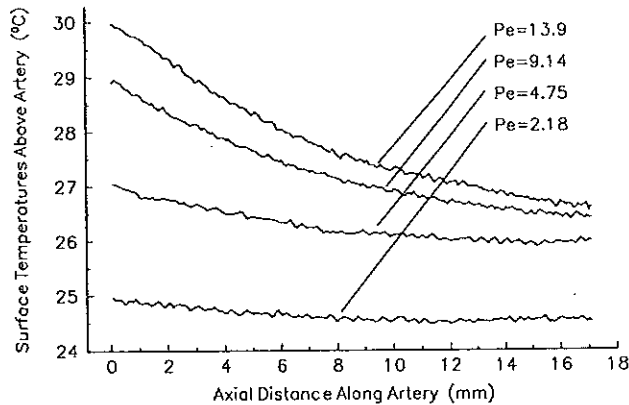

FIGURE 5. Temperature profiles along the central arteriole and venule of the cremaster at four different blood flow rates. $z^* = 0$ mm is the proximal end of the artery as it enters the tissue bath, and $z^* = 17$ mm is the distal end of the recording area.

MATHEMATICAL MODEL

Formulation

In this section, the essential features of the three-dimensional mathematical model used to describe the boundary value problem shown in Fig. 2b are summarized and the differences between this model and that of Zhu and Weinbaum (28) are highlighted. Two vessels embedded in a thin tissue layer of thickness $H^* = H_1^* + H_2'^*$ were examined. The tissue is supported by a thin glass plate of thickness H_g^*.

The principal simplifying assumptions of the model are as follows: both the flow and temperature fields are steady, and the velocity profiles in the blood vessels are parabolic; the glass plate in the cross-sectional plane can be converted into an equivalent tissue layer of thickness $H_g \, k_t/k_g$ so that the boundary value problem can be simplified into an equivalent tissue layer of thickness $H^* = H_1^* + H_2^* = H_1^* + (H_2'^* + H_g^* k_t/k_g)$; and to accurately describe the axial conduction for the new cross-sectional plane, the conductivity in the axial direction can be converted into an equivalent value k_m, if one assumes equal axial temperature gradients in the glass and the tissue regions. k_m is defined in the following expression:

$$k_m\left(H_1^* + H_2'^* + H_g^* \frac{k_t}{k_g} \right) = k_t(H_1^* + H_2'^*) + k_g H_g^*,$$

$$\text{or } \frac{k_m}{k_t} = \frac{H_1^* + H_2'^* + H_g^* k_g/k_t}{H_1^* + H_2'^* + H_g^* k_t/k_g}$$

To simplify the complexity caused by axial conduction, the axial conduction term in the tissue energy equation, $\partial^2\theta_t/\partial z^2$, is approximated by its average value, $d^2\theta_{t,ave}/dz^2$, defined below in Eq. 10, whereas the axial conduction in the blood vessels is neglected, because the cross-sectional area of the blood vessels is small compared to that of the tissue. The temperature gradient $\delta\theta_{a,v}/\delta z$ in the convective term of the vessel energy equations can be approximated by the axial gradient of the vessel bulk temperatures, $d\theta_{ab,vb}/dz$, as justified previously (29). The cross-sectional plane is uniform in the axial direction, and perfusion bleed-off from the supply artery-vein pair is neglected. This simplification is discussed in detail below. The basic geometry, symbols, and coordinate system are shown in Fig. 2b.

Nondimensional parameters are introduced as follows:

$$\rho_a = \frac{\rho_a^*}{\rho_{ar}^*}, \; \rho_v = \frac{\rho_v^*}{\rho_{ar}^*}, \; \rho_{vr} = \frac{\rho_{vr}^*}{\rho_{ar}^*}, \; x = \frac{x^*}{\rho_{ar}^*}, \; y = \frac{y^*}{\rho_{ar}^*},$$

$$z = \frac{z^*}{\rho_{ar}^*(k_m/k_t)^{0.5}} , \; H_{1,2} = \frac{H_{1,2}^*}{\rho_{ar}^*}, \; D = \frac{D^*}{\rho_{ar}^*},$$

$$l = \frac{l^*}{\rho_{ar}^*}, \quad L = \frac{L^*}{\rho_{ar}^*}, \quad Pe = \frac{2\gamma_f C_f \rho_{ar}^* u_a}{k_f},$$

$$Bi_{1,2} = \frac{h_{1,2}\rho_{ar}^*}{k_t}, \quad \theta_{a,v,t} = \frac{T_{a,v,t} - T_\infty}{T_{a0} - T_\infty}, \quad \bar{u} = \frac{u_v}{u_a}$$

where the subscripts a and v refer to artery and vein, *asterisks* denote dimensional variables, and ρ_{ar}^* and ρ_{vr}^* are the dimensional radii of the artery and vein. Note that z is scaled by $\rho_{ar}^*(k_m/k_t)^{0.5}$ rather than by $Pe\rho_{ar}^*$, as it was scaled in the model of Zhu and Weinbaum (28). This change allows one to eliminate the conductivity ratio in the governing equation for the tissue. Introducing the above assumptions, one obtains the following simplified dimensionless governing equations and boundary conditions for the vessels and the tissue:

$$\frac{1}{\rho_a}\frac{\partial}{\partial \rho_a}\left(\rho_a \frac{\partial \theta_a}{\partial \rho_a}\right) + \frac{1}{\rho_a^2}\frac{\partial^2 \theta_a}{\partial \phi_a^2} = Pe(1 - \rho_a^2)\frac{d\theta_{ab}}{dz}, \quad \rho_a \leqslant 1$$

(1)

$$\frac{1}{\rho_v}\frac{\partial}{\partial \rho_v}\left(\rho_v \frac{\partial \theta_v}{\partial \rho_v}\right) + \frac{1}{\rho_v^2}\frac{\partial^2 \theta_v}{\partial \phi_v^2} =$$

$$Pe\bar{u}\left(1 - \frac{\rho_v^2}{\rho_{vr}^2}\right)\frac{d\theta_{vb}}{dz}, \quad \rho_v \leqslant \rho_{vr}$$

(2)

$$\frac{\partial^2 \theta_t}{\partial x^2} + \frac{\partial^2 \theta_t}{\partial y^2} = -\frac{d^2 \theta_{tave}}{dz^2}, \quad \rho_a > 1, \ \rho_v > \rho_{vr},$$

(3)

$$-D \leqslant x \leqslant D, \quad -H_2 \leqslant y \leqslant H_1$$

$$\begin{cases} \theta_a = \theta_t, \\ K'\dfrac{\partial \theta_a}{\partial \rho_a} = \dfrac{\partial \theta_t}{\partial \rho_a}, \end{cases} \quad \rho_a = 1$$

(4)

$$\begin{cases} \theta_v = \theta_t, \\ K'\dfrac{\partial \theta_v}{\partial \rho_v} = \dfrac{\partial \theta_t}{\partial \rho_v}, \end{cases} \quad \rho_v = \rho_{vr}$$

(5)

$$\frac{\partial \theta_t}{\partial y} = \mp Bi_{1,2}\theta_t, \quad y = \pm H_{1,2}$$

(6)

For a preparation in which the width $2D$ is much larger than the tissue thickness H, it is reasonable to assume that there is no heat flow across the boundaries at $x = \pm D$. Therefore, the adiabatic condition is required:

$$\frac{\partial \theta_t}{\partial x} = 0 \quad x = \pm D$$

(7)

In Eqs. 1 and 2, θ_{ab}, θ_{vb}, and $\theta_{t,ave}$ are the artery bulk temperature, vein bulk temperature, and average tissue temperature, respectively. These temperatures are defined as

$$\theta_{ab} = \frac{2}{\pi}\int_{-\pi}^{\pi}\int_0^1 \theta_a(1 - \rho_a^2)\rho_a d\rho_a d\phi_a$$

(8)

$$\theta_{vb} = \frac{2}{\pi \rho_{vr}^2}\int_{-\pi}^{\pi}\int_0^{\rho_{vr}}\theta_v\left(1 - \frac{\rho_v^2}{\rho_{vr}^2}\right)\rho_v d\rho_v d\phi_v$$

(9)

$$\theta_{tave} = $$

$$\frac{1}{2D(H_1 + H_2) - \pi - \pi\rho_{vr}^2}\iint_{\text{tissue region}}\theta_t(x,y,z)dx\,dy$$

(10)

The fundamental differences between the above formulation and that in the model of Zhu and Weinbaum (28) are that axial conduction is treated in the tissue (right side of Eq. 3) and the effective thickness of the tissue in the lower region has been increased to include the glass plate.

Solution for Countercurrent Flow

A theoretical solution to the complicated boundary value problem summarized above can be obtained by modifying the solution procedure outlined by Zhu and Weinbaum (28). The simplifications introduced in the governing Eqs. 1, 2, and 3 and the boundary conditions enable one to separate variables and solve the boundary value problem in the cross-sectional plane independent of the boundary value problem in the z direction. First a Green's function or fundamental solution must be developed for a line source arbitrarily positioned within the tissue-vessel region. Then, the solution for two countercurrent vessels undergoing countercurrent heat exchange must be constructed by superposing the fundamental solutions. Finally, the boundary value problem for the axial interaction is solved to determine the vessel bulk temperatures and the average tissue temperature.

The fundamental solution or Green's function $W(x,y;\xi,\eta)$ satisfies Laplace's equation in the rectangular region, $-D < x < D$ and $-H_2 < y < H_1$, except for the source point (ξ,η) arbitrarily located inside the region. This solution also satisfies the boundary conditions in Eqs. 6 and 7. The derivation for this Green's function is presented in Appendix 1 of the study by Zhu and Weinbaum (28). The solution for W is

$$W = (C_1 y + C_2) + \sum_{n=1}^{\infty}\frac{1}{D}\cos[\sqrt{\lambda_n}$$

$$(\xi - D)]\cos[\sqrt{\lambda_n}(x - D)][A_1 e^{\sqrt{\lambda_n}y}$$

$$+ B_1 e^{-\sqrt{\lambda_n}y}] \quad y \geqslant \eta$$

$$W = (D_1 y + D_2) + \sum_{n=1}^{\infty}\frac{1}{D}\cos[\sqrt{\lambda_n}$$

$$(\xi - D)]\cos[\sqrt{\lambda_n}(x - D)][A_2 e^{\sqrt{\lambda_n}y}$$
$$+ B_2 e^{-\sqrt{\lambda_n}y}] \quad y \leq \eta \tag{11}$$

where A_i, B_i, C_i, and D_i, ($i = 1,2$) are constants that depend on the Biot number and the tissue geometry, and are listed in (A.8) and (A.10) of Appendix 1 of the study by Zhu and Weinbaum (27), and the eigenvalue $\lambda_n = (n\pi/2D)^2$.

The solution for the countercurrent artery-vein pair is decomposed into a particular solution and a general solution. These expressions are

$$\theta_a = (\rho_a^2 - \frac{1}{4}\rho_a^4 - \frac{3}{4})\frac{Pe}{4}\frac{d\theta_{ab}}{dz} + \frac{a_{a0}}{2} + \sum_{j=1}^{\infty} a_{aj}\rho_a^i \cos(j\phi_a)$$
$$+ b_{aj}\rho_a^i \sin(j\phi_a) \tag{12}$$

$$\theta_v = \left(\rho_v^2 - \frac{1}{4}\frac{\rho_v^4}{\rho_{vr}^2} - \frac{3}{4}\rho_{vr}^2\right)\frac{Pe\bar{u}}{4}\frac{d\theta_{vb}}{dz} + \frac{a_{v0}}{2}$$
$$+ \sum a_{vj}\rho_v^i \cos(j\phi_v) + b_{vj}\rho_v^i \sin(j\phi_v) \tag{13}$$

Similarly, the tissue temperature also can be decomposed into a particular solution and a general solution; $\theta_t = \theta_{pt} + \theta_{ht}$. V_{pt} is given by

$$\theta_{pt} = -\frac{d^2\theta_{tave}(z)}{dz^2}\left(\frac{y^2}{2} + I_1 y + I_2\right) \tag{14}$$

where, the coefficients I_1 and I_2 are only functions of $H_{1,2}$ and $Bi_{1,2}$ and are given in the Appendix. This particular solution is not needed in the model used by Zhu and Weinbaum (28), because the right side of Eq. 3 is homogeneous. θ_{ht} satisfied Laplace's equation in the tissue region and boundary conditions in Eqs. 6 and 7. The general solution for the tissue can be constructed by placing two anisotropic line sources at the centers of the artery and vein with strengths C_{sa} and C_{sv}, respectively. Therefore, θ_{ht} is a linear combination of Green's functions representing these sources. The tissue temperature is expressed by

$$\theta_t =$$
$$C_{sa}W(x,y;\xi_a,\eta_a) + C_{sv}W(x,y;\xi_v,\eta_v) + \theta_{pt}(y,z) \tag{15}$$

where (ξ_a,η_a) and (ξ_v,η_v) are the coordinates of the artery and the vein, respectively, in Eq. 11 for $W(x,y;\xi,\eta)$. Note that the tissue temperature also satisfied the governing Eq. 3 and boundary conditions Eqs. 6 and 7.

As shown by Zhu and Weinbaum (28), the coefficients a_{aj}, b_{aj}, a_{vj}, b_{vj}, C_{sa}, and C_{sv} in Eqs. 12 and 13 were determined by the matching conditions in Eqs. 4 and 5 for the continuity of temperature and heat flux on the vessel surfaces. Only the expressions for C_{sa}, C_{sv}, a_{a0}, and a_{v0} are needed for our final results

$$C_{sa} = \frac{K'\pi Pe}{2}\frac{d\theta_{ab}}{dz} + \pi\frac{d^2\theta_{tave}}{dz^2} \tag{16a}$$

$$C_{sv} = \frac{K'\pi Pe\rho_{vr}^2\bar{u}}{2}\frac{d\theta_{vb}}{dz} + \rho_{vr}^2\pi\frac{d^2\theta_{tave}}{dz^2} \tag{16b}$$

$$a_{a0} = \frac{1}{\pi}\int_{-\pi}^{\pi}[C_{sa}W(x,y;\xi_a,\eta_a) + C_{sv}W(x,y;\xi_v,\eta_v)$$
$$+ \theta_{pt}]|_{\rho_a=1}d\phi_a \tag{17a}$$

$$a_{v0} = \frac{1}{\pi}\int_{-\pi}^{\pi}[C_{sa}W(x,y;\xi_a,\eta_a) + C_{sv}W(x,y;\xi_v,\eta_v)$$
$$+ \theta_{pt}]|_{\rho_v=\rho_{vr}}d\phi_v \tag{17b}$$

It can be shown, as in Reference 28, that the solution is exact when $K' = 1$, whereas, when $K' \neq 1$, the solution is approximate, because it satisfies the heat flux continuity on the vessel surface globally rather than locally.

θ_{ab}, θ_{vb}, and θ_{tave} remain to be determined. Substituting Eqs. 12, 13, and 15 into the expressions for θ_{ab}, θ_{vb}, and θ_{tave}, respectively, yielded

$$\theta_{ab} = -\frac{11Pe}{96}\frac{d\theta_{ab}}{dz} + \frac{a_{a0}}{2} \tag{18}$$

$$\theta_{vb} = -\frac{11Pe}{96}\bar{u}\rho_{vr}^2\frac{d\theta_{vb}}{dz} + \frac{a_{v0}}{2} \tag{19}$$

$$\theta_{tave} = \iint_{tissue\ region}\left\{\left[\frac{C_{sa}W(x,y;\xi_a,\eta_a) + C_{sv}W(x,y;\xi_v,\eta_v)}{2D(D(H_1 + H_2) - \pi - \pi\rho_{vr}^2}\right]\right.$$
$$\left.+ \left[\frac{d^2\theta_{tave}}{dz^2}\frac{-Pe^2(y^2 + I_1y + I_2)}{2D(H_1 + H_2) - \pi - \pi\rho_{vr}^2}\right]\right\}d\Omega \tag{20}$$

Note that a_{a0}, a_{v0}, C_{sa} and C_{sv} are linear combinations of $d\theta_{ab}/dz$, $d\theta_{vb}/dz$, and $d^2\theta_{tave}/dz^2$.

Substituting the expressions for a_{a0}, a_{v0}, C_{sa}, and C_{sv} into Eqs. 18, 19, and 20, yielded

$$\theta_{ab} = A_{11}\frac{d\theta_{ab}}{dz} + A_{12}\frac{d\theta_{vb}}{dz} + A_{13}\frac{d^2\theta_{tave}}{dz^2} \tag{21}$$

$$\theta_{vb} = A_{21}\frac{d\theta_{ab}}{dz} + A_{22}\frac{d\theta_{vb}}{dz} + A_{23}\frac{d^2\theta_{tave}}{dz^2} \tag{22}$$

$$\theta_{tave} = A_{31}\frac{d\theta_{ab}}{dz} + A_{32}\frac{d\theta_{vb}}{dz} + A_{33}\frac{d^2\theta_{tave}}{dz^2} \tag{23}$$

where A_{11-33} are listed in the Appendix. If axial conduction is neglected, as it was by Zhu and Weinbaum (28), one obtains a reduced set of equations involving only θ_{ab} and θ_{vb}.

The three coupled equations (Eqs. 21, 22, and 23) for

the vessel bulk temperatures and the average tissue temperature are linear, ordinary, differential equations that can be solved easily once the appropriate boundary conditions in the axial direction are specified. For countercurrent flow, this requires that only the artery bulk inlet temperature be prescribed, because, as $z \to \infty$, both the venous bulk temperature and the artery bulk temperature approach T_∞. For the tissue region, the average tissue entrance temperature, θ_{t0}, can differ from the arterial inlet temperature, $\theta_{a0} = 1$. These boundary conditions are given by

$$\theta_{ab} = 1 \quad z = 0 \tag{24a}$$

$$\theta_{tave} = \theta_{t0} \quad z = 0 \tag{24b}$$

$$\theta_{ab}, \theta_{vb}, \theta_{tave} \to 0 \quad z \to \infty \tag{24c}$$

The general solution of Eqs. 21, 22, and 23 is an eigenfunction of the form of $e^{E_i z}$, in which the eigenvalues E_i can be negative, positive, or a complex variable and θ_{ab}, θ_{vb}, and θ_{tave} are arbitrary combinations of all possible eigenfunctions. Because of the boundary condition (Eq. 24c), one can exclude eigenfunctions with the positive eigenvalue B_i. One finds that θ_{ab}, θ_{vb}, and θ_{tave} must have the functional forms

$$\theta_{ab} = A_1 e^{-E_1 Z} + A_2 e^{-E_2 Z} \tag{25a}$$

$$\theta_{vb} = C_{11} A_1 E^{-E_1 Z} + C_{12} A_2 E^{-E_2 Z} \tag{25b}$$

$$\theta_{tave} = C_{21} A_1 e^{-E_1 Z} + C_{22} A_2 e^{-E_2 Z} \tag{25c}$$

where $C_{11,12,21, \text{ and } 22}$ are coefficients calculated from Eqs. 21, 22, and 23. The unknown coefficients A_1 and A_2 are determined by boundary conditions (Eqs. 24a and 24b).

Conduction Shape Factor Between the Artery and the Vein in the Cross-Sectional Plane. The expression for the conduction shape factor significantly simplifies for the case of equal size blood vessels symmetrically positioned relative to the vertical axis. If one analyzes the expressions for the coefficients in Eqs. 21, 22, and 23, after requiring that the mass flow in each vessel be the same ($\rho_{vr}^2 \bar{u} = -1$), one finds the following:

$$A_{11} = -A_{22} = Pe \left(-11/96 + \frac{K'\pi}{2} \overline{W}_{a-a} \right)$$

$$A_{12} = -A_{21} = \frac{-PeK'\pi}{2} \overline{W}_{v-a}$$

$$A_{13} = A_{23}$$

where the coefficients in the above relations are listed in the Appendix. Subtracting Eq. 22 from Eq. 21, one obtains

$$\theta_{ab} - \theta_{vb} = (A_{11} + A_{12}) \frac{d(\theta_{ab} + \theta_{vb})}{dz} \tag{26}$$

In Reference 3, Baish *et al.* introduced two shape factors, σ_Δ and σ_Σ, that describe conduction between the artery and the vein, and between both vessels and the tissue, respectively. σ_Δ was obtained by adding Eqs. 10 and 11 in reference 3, which is given by

$$\sigma_\Delta = \frac{\pi \gamma_b C_b \rho_{ar}^{*2} \bar{u}}{2k_t (T_{ab} - T_{vb})} \frac{d(T_{ab} + T_{vb})}{dz^*} \tag{27}$$

Introducing the dimensionless parameters and comparing Eqs. 26 and 27, one obtains the following expression for σ_Δ:

$$\sigma_\Delta = -\frac{P_e \pi}{4(A_{11} + A_{12})} = \frac{1}{2K'\overline{W}_{va} - 2\overline{W}_{aa} + 11/(24\pi)} \tag{28}$$

Thermal Equilibrium Length in the Axial Direction. Once the vessel bulk temperatures and the average tissue temperature are known, one can obtain expressions for the vessel temperatures at any location in the vessel region from Eqs. 12 and 13. For the tissue temperature, one substitutes Eqs. 25a, 25b, and 25c into Eq. 15 and obtains

$$\theta_t(x,y,z) = F_1(x,y) e^{-E_1 z} + F_2(x,y) e^{-E_2 z} \tag{29}$$

where $F_1(x,y)$ and $F_2(x,y)$ are functions of the vessel-tissue geometry and Pe and are listed in the Appendix.

The tissue axial thermal equilibration length is the distance over which the tissue temperature decreases by a factor of e. Comparing Eqs. 25a and 29, one finds that the thermal equilibration length calculated from the surface temperature is not the same as that of the feeding artery, although they are related. Only when the initial average tissue temperature θ_{tave} is equal to either C_{21} or C_{22} can the tissue temperature be reduced to an expression containing only a single decaying mode. For these special conditions, the tissue temperature and vessel temperature follow the same temperature decay pattern in the axial direction. For the more general case, the tissue temperature has two decaying modes. However, the difference of thermal equilibration lengths between vessel and tissue will be small if the tissue thickness H is much smaller than the tissue width $2D$ and the temperature gradient across the tissue thickness is small. Therefore, we conclude that the thermal equilibration length calculated from the tissue surface temperature is a good approximation of that of the feeding blood vessels. The tissue temperature distribution in the cross-sectional plane at any z is obtained from Eq. 29.

PARAMETERS

The thermal properties of the preparation and the surroundings and the geometrical parameters describing the

tissue preparation are summarized in Table 1. The convective coefficient h ranges from 5 to 25 $W/m^2°C$ and corresponds to free convection conditions. The ranges for most of the geometrical parameters were obtained from these experiments on the rat cremaster muscle.

When vasoactive agents are introduced, the diameter, spacing, and Pe of the vessels change. An important advantage of this two-dimensional preparation is that all of these parameters can be measured carefully and used as input in this theoretical model. Typically, the diameter of a 1A vessel varied by a factor of approximately two when NE and sodium nitroprusside are used, and the Pe varied by an order of magnitude. There was little change in the spacing of the tissue between the vessels, because the tissue is nearly incompressible, and, therefore, the change in l is primarily caused by the increase in diameter.

RESULTS

Axial Variation of Artery, Vein, and Average Tissue Temperature

In Figs. 6–9, the radii of the feeding arteriole and venule were 50 μm, and the preparation thickness was 150 μm. The ratio of equivalent axial thermal conductivity to tissue conductivity, k_m/k_t, was found to be 2.56. Therefore, $H_1 = 1.5$ and $H_2 = 3.214$. For equal or unequal vessel pairs, the ratio of artery and vein velocity, $\bar{u}$, was determined by requiring that the mass flow in each vessel be the same.

We have examined the effects of several factors on axial temperature variation and thermal equilibration length, such as convective coefficient h of the surroundings, the inlet average tissue temperature θ_{t0}, and the blood flow Peclet number Pe. For $Pe = 8$, Fig. 6 shows how the inlet average tissue temperature θ_{t0} influences the axial temperature variation in the vessels and tissue. Note from Eqs. 25a, 25b, and 25c that θ_{t0} affects the axial distributions by altering the weighting of the two eigenfunctions in the solution. An elevation of the tissue inlet temperature means that more of the heat leaving the feeding arteriole can return to the venule and, thus, be prevented from being lost to the surroundings. Therefore, the larger θ_{t0}, the longer the thermal equilibration length of the feeding artery and the warmer the blood in the return-

TABLE 1. Key parameters.

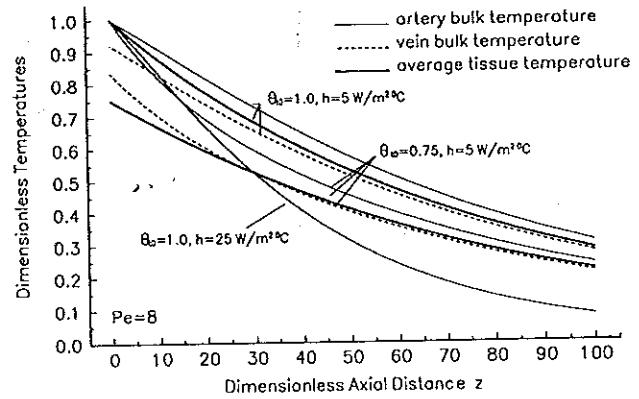| Thermal properties	Geometric properties
$\gamma_f = 1000$ kg/m³	$\rho_{ar}^* = 40–75$ μm
$C_f = 4180$ J/kg°C	$\rho_{vr}^* = 40–125$ μm
$k_f = k_t = 0.6$ W/m°C	$H^* = 100–400$ μm
$k_g = 1.4$ W/m°C	$H_g^* = 200$ μm
$h = 5–25$ W/m²°C	$D^* = 50$ mm
	$Pe = 1–15$

FIGURE 6. The effect of inlet tissue temperature and convection coefficient on the axial temperature distribution. Note that $Pe = 8$, and the dimensionless axial distance z is scaled by $\rho_{ar}^*(k_m/k_t)^{0.5}$. The dimensionless artery bulk temperature at the entrance always is equal to 1.

ing vein. Observe in Fig. 6 that the average tissue temperature θ_{tave} closely follows the vein bulk temperature θ_{vb} and, except near the inlet, lies between the artery and vein bulk temperatures. Figure 6 also shows that the axial variation of the dimensionless artery bulk temperature θ_{ab} is altered significantly by changing the convective coefficient h. For $Pe = 8$ and $\theta_{t0} = 1$, the dimensionless thermal equilibration length L is reduced from 95 to 40 when the convective coefficient h is increased from 5 to 25 $W/m^2°C$. The axial thermal equilibration length L^* decreases from 7.6 to 3.2 mm for this increase in h.

The influences of the blood flow Peclet number and the glass plate on the thermal equilibration of the artery are illustrated in Fig. 7. A comparison of the thin solid line and the long dashed line in Fig. 7 reveals that the thermal equilibration length is increased by more than a factor of two as a result of the presence of the supporting glass slide. There are two principal sources for the axial temperature decay; one is axial conduction, and the other is
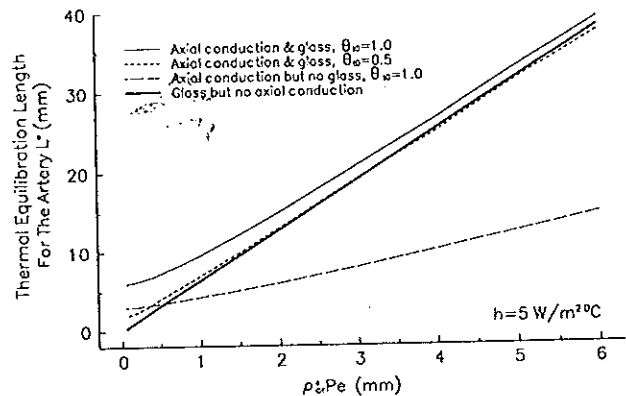

FIGURE 7. The effects of axial conduction and countercurrent flow on the axial thermal equilibration length for different ρ_{ar}^*Pe.

blood flow. Note that the thermal equilibration length is proportional to the blood flow Peclet number when axial conduction can be neglected (28), as shown by the heavy solid line in Fig. 7. However, in our modified model, which considers axial conduction, the thermal equilibration length L increases slowly with blood flow Peclet number when $\rho_{ar}^* Pe$ is less than 1 mm. Figure 8 shows the percentage contribution of countercurrent flow to the axial thermal equilibration at two values of tissue inlet temperature, $\theta_{t0} = 1.0$ and $\theta_{t0} = 0.5$. L_{conv} is the thermal equilibration length when axial conduction is neglected (28), and $L_{cond+conv}$ is the thermal equilibration length when both countercurrent flow and axial conduction are considered. Figure 7 shows that axial conduction is the dominant mode of axial thermal equilibration when $\rho_{ar}^* Pe < 1$ mm. For $1 < \rho_{ar}^* Pe < 3$ mm, the effect of countercurrent blood flow becomes comparable to axial conduction, whereas, when $\rho_{ar}^* Pe > 3$ mm, countercurrent heat exchange becomes dominant. This is evident in Fig. 8, which shows that, for both values of θ_{t0}, the thermal equilibration length caused by countercurrent flow accounted for at least 90% of the total equilibration length when $\rho_{ar}^* Pe > 3$ mm. Figures 7 and 8 also show that, at high blood perfusion rates, the inlet average tissue temperature θ_{t0} has less influence on the axial thermal equilibration, and the axial thermal equilibration length is proportional to the blood flow Peclet number, as was predicted previously by Zhu and Weinbaum (28).

Surface Temperature Profiles

The surface temperature is obtained from Eq. 29 by setting $y = H_1$. Because the temperature profile across the tissue thickness is almost uniform for small H, the trends

for the axial temperature decay at the surface are similar to those for θ_{ab}. Therefore, the effects discussed in Fig. 6 and 7 were nearly the same for the axial surface temperature profiles as they were for the axial temperature profile of the feeding artery.

Figure 9 is a plot of the surface temperature profiles for different θ_{t0}, at two axial locations, one at the entrance, $z = 0$, and one far downstream, $z = 70$, for two values of h. Figure 9 shows that, at the two higher values of θ_{t0}, $\theta_{t0} = 0.9$ and 1.0, less heat is lost from the artery to the environment and the surface thermal fluctuation because the vessels are smaller near the entrance. At higher tissue temperatures, there is a significant countercurrent rewarming of the vein. For $\theta_{t0} < 0.9$, there is a single maximum with no significant minimum for the vein. When the axial distance z increases from 0 to 70, the shapes of the temperature profiles are similar, and θ_{t0} only affects the level of local average tissue temperature. It can been seen that the location of the surface maximum lies right above the artery. Therefore, the horizontal location of the artery can be determined from the maximum in the surface profiles. Figure 9 also shows the initial surface profile for $h = 25$ $W/m^2°C$ for $\theta_{t0} = 0.75$. Changing h affects the axial decay but does not have a significant influence on the initial surface temperature distribution.

Comparison of the Experimental Data and the Theoretical Results

The unknown parameter required to compare the experimental data and the theoretical results is the convective coefficient h. Although h cannot be measured directly in our experiments, we can estimate its value by comparing the equilibration length predicted by the theoretical model with that measured from the axial decay of the surface temperature field. For this comparison, we selected $\theta_{t0} = \theta_{x0}$ on the basis of the results shown in Fig.
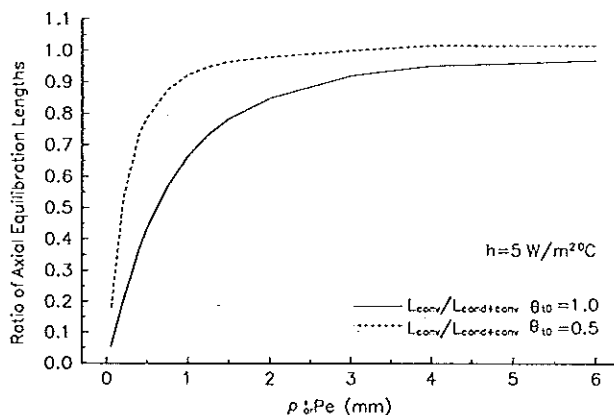

FIGURE 8. The percentage contributions of countercurrent flow and axial conduction to the axial thermal equilibration length at two values of tissue inlet temperature $\theta_{t0} = 0.5$ and $\theta_{t0} = 1.0$. L_{conv} is the thermal equilibration length neglecting axial conduction (heavy solid line in Fig. 7) and $L_{cond+conv}$ is the thermal equilibration length considering axial conduction (solid and short dashed lines in Fig. 7).
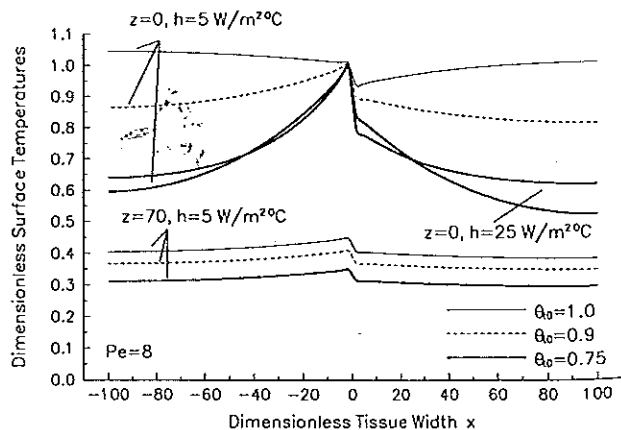

FIGURE 9. Surface temperature profiles at different axial locations ($z = 0, 70$) for different inlet tissue temperatures and convective coefficients ($Pe = 8$).

6. Figure 10 compares the theoretical predictions for the axial surface temperature distribution for one experiment in which results were obtained for four different values of Pe by drug-induced vasodilation and vasoconstriction. For this comparison, the diameters of the vessels and their spacings were changed in the model to agree with the experimental measurements at each Pe. When h is selected as 6 W/m²°C, the temperature distributions predicted by the model correlate very closely with the experimental data for all four blood flow Peclet numbers. Although one might choose h to fit one axial profile, the ability to predict all four profiles with the same h is strong support for the validity of the model, because h does not change during the course of one experiment. This value of h is reasonable for free convection on a horizontal tissue surface in air.

The theoretical and experimental surface temperature profiles normal to the main cremaster vessels are shown in Fig. 11 for one of the trials ($Pe = 7.8$) at four axial locations. The theoretical results predict a maximum temperature above the feeding arteriole and an almost uniform temperature distribution in the horizontal direction. The theoretical predictions are consistent with the experimental measurements. However, the small but steep temperature gradient between the countercurrent artery-vein pair predicted by the theoretical model was not clearly visible in these experiments. This small temperature difference may have been camouflaged by the limitation in the spatial resolution of the experimental measurements or by the simplifications in the model discussed below.

Although the diameters and inflow Pe in the 1A vessels were measured carefully and used as input conditions in the model, vessel branchings were neglected in the analysis. The first 2A branching typically was observed to occur 5–7 mm from the entrance of the 1A vessel pair. These 2A vessels have a diameter that is typically 60% of
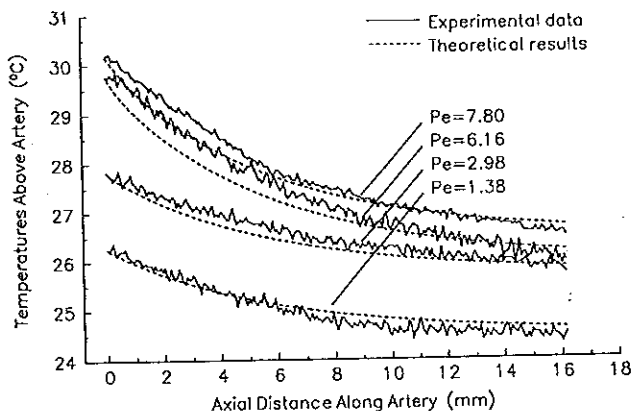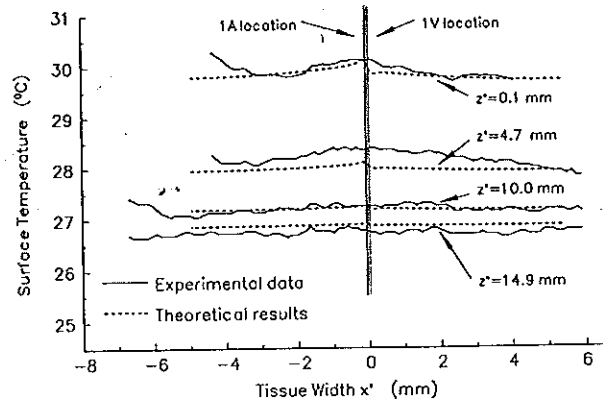
FIGURE 11. Comparisons of the theoretical and experimental results for the surface temperature profiles at four different axial locations.

that of their parent 1A vessels, and, as shown by Zhu et al. (27), they have a flow that roughly satisfies the condition that $Q/(2\rho_{ar}^*)^3$ is a constant. The flow Q in the 2A vessel, therefore, is approximately 20% of that of its parent vessel, and its Pe is approximately 33% of that of its parent vessel. Therefore, the flow in the 2A vessel is conduction dominant, and the idealization in the model that flow in the 1A vessel is constant, although not true, is not an unrealistic simplification.

Comparison of the Theoretical Model and the Weinbaum-Jiji Equation

The sophisticated model developed in this study provides an accurate basis for examining the validity of simpler one-dimensional models in which an effective conductivity k_{eff} is used to describe the enhancement in conductivity caused by blood flow. In particular, one can compare the results of this model with those obtained from the Weinbaum-Jiji equation. By applying the Weinbaum-Jiji equation (21) to the tissue preparation (without glass plate) and introducing the dimensionless parameters shown above, one can obtain a simple one-dimensional energy equation for $\theta_{tave}(z)$ as follows:

$$\frac{d\theta_{tave}^2(z)}{dz^2} \frac{k_{eff}}{k_t} = \frac{2Bi}{H^2} \theta_{tave}(z), \qquad \frac{k_{eff}}{k_t} = 1 + \frac{n\pi^2 Pe^2 \rho_{ar}^{*2}}{4\sigma_\Delta} \tag{30}$$

where σ_Δ is the condition shape factor for heat transfer between two vessels at different temperatures in the cross-sectional plane, and n is the countercurrent vessel pair number density per unit of cross-sectional area, which is equal to $1/(2DH\rho_{ar}^{*2})$. The solution of Eq. 30 for the tissue temperature is

$$\theta_{tave} = \theta_{t0} e^{-z/L}$$

where the thermal equilibrium length L^* is

FIGURE 10. Comparison of the theoretical and experimental results for axial surface temperature decay at different blood flow Peclet numbers.

blood vessels that lie between 160 and 240 μm in diameter for normal flow conditions (27). Countercurrent heat transfer between the blood and the tissue dominates heat transfer in blood vessels when $\rho_{ar}^{*}Pe > 3$ mm, and, for these conditions, heat conduction can be neglected.

In our previous study (27), we predicted the enhancement in the effective conductivity k_{eff}/k_t by measuring the changes in flow and diameter in 1A to 4A blood vessels due to hyperthermia and drug-induced vasodilation and applying the Weinbaum-Jiji expression for k_{eff} (Eq. 30) for each vessel generation. Results have shown that countercurrent blood flow in vessels less than 75 μm in diameter does not significantly contribute to k_{eff}/k_t. However, by extrapolating the experimental data, we (27) predicted previously that significant enhancement should start to occur for vessels larger than 80 μm diameter. Our predictions in Reference 27 reveal that a twofold increase in the effective conductivity k_{eff}/k_t will occur when $\rho_{ar}^{*}Pe$ is approximately 1.5 mm and that a sixfold increase will occur when $\rho_{ar}^{*}Pe = 3$ mm. The transition from conduction- to convection-dominated axial transport between $\rho_{ar}^{*}Pe$ equal to 1 and 3 mm predicted by this model is, therefore, in close agreement with the theoretical predictions for k_{eff}/k_t in Reference 27.

With the use of a newly derived shape factor for conduction in the cross-sectional plane of the tissue preparation, we compared the thermal equilibration lengths calculated by the Weinbaum-Jiji model (21) and the more accurate three-dimensional model. This newly derived conduction shape factor is a function of the local geometry and the convective coefficient h and is found to be much smaller than that calculated from the widely known bipolar solution (9) for perfect countercurrent heat exchange. For $l = 3.0$ and $H = 3.0$, the newly derived conduction shape factor is approximately one-third of the old one (9) and is found to be almost independent of the convection coefficient h. The axial thermal equilibration lengths of the tissue calculated by applying a simple one-dimensional Weinbaum-Jiji model to the tissue preparation are found to have similar trends to those predicted by the more accurate three-dimensional theoretical model. When compared with the three-dimensional model, we found that the Weinbaum-Jiji equation correctly predicts the shape of the axial thermal equilibration length *versus* $\rho_{ar}^{*}Pe$ curve, although it underestimates k_{eff} for larger blood perfusion rates. This underestimation of k_{eff} can be traced to the assumption in the Weinbaum-Jiji equation that the gradient of the mean tissue temperature is equal to the gradient of the mean blood temperature.

Asymptotic analyses presented in References 8 and 22 rigorously show that the validity of this assumption requires that $\epsilon = L^{*}/L^{*}_{length}$, the normalized thermal equilibration length of the blood vessels, be <0.2. Here, L^{*}_{length} is either the vessel length or the characteristic

length of the tissue temperature gradient. When $\rho_{ar}^{*}Pe < 1$ mm, the conditions of the present experiments, the thermal equilibration lengths of the blood vessels in the countercurrent network are small compared with the length scale of the macroscopic temperature gradients in the tissue. Under these conditions, the Weinbaum-Jiji equation is in good agreement with the more accurate three-dimensional model. However, for $\rho_{ar}^{*}Pe > 1$ mm, the accuracy of the Weinbaum-Jiji equation depends on the value of h. For small h, the decay length is longer, and the vessel bulk temperatures follow the tissue temperature gradient closely (see Fig. 6). In this case, the thermal equilibration between the artery-vein pairs does not depart significantly from nearly perfect countercurrent exchange, and the Weinbaum-Jiji model is a good approximation, although $\rho_{ar}^{*}Pe > 1$ mm. However, for larger h, the tissue decay length is short, ϵ is >0.2, and the criterion for the validity of the Weinbaum-Jiji equation is exceeded.

REFERENCES

1. Anderson, G. T., and J. W. Valvano. A small artery heat transfer model for self-heated thermistor measurements of perfusion in the kidney cortex. *J. Biomech. Eng.* 116:71–78, 1994.

2. Baez, S. An open cremaster muscle preparation for the study of blood vessels by *in vivo* microscopy. *Microvasc. Res.* 5:384–394, 1973.

3. Baish, J. W., P. S. Ayyaswamy, and K. R. Foster. Heat transport mechanism in vascular tissues: a model comparison. *J. Biomech. Eng.* 108:324–331, 1986a.

4. Baish, J. W., P. S. Ayyaswamy, and K. R. Foster. Small-scale temperature fluctuations in perfused tissue during local hyperthermia. *J. Biomech. Eng.* 108:246–250, 1986b.

5. Baker, M., and H. Wayland. On-line volume flow rate and velocity profile measurement for blood in microvessels. *Microvasc. Res.* 7:131–134, 1974.

6. Bau, H. H., and S. S. Sadhal. Heat losses from a fluid flowing in a buried pipe. *Int. J. Heat Mass Transfer* 25:1621–1629, 1982.

7. Bazett, H. C., I. Love, M. Newton, I. Eisenberg, R. Day, and R. Forest. Temperature changes in blood flowing in the arteries and veins in man. *J. Appl. Physiol.* 1:3–19, 1948.

8. Charny, C. K., S. Weinbaum, and R. L. Levin. An evaluation of the Weinbaum-Jiji bioheat equation for normal and hyperthermic conditions. *J. Biomech. Eng.* 112:80–87, 1990.

9. Chato, J. C. Heat transfer to blood vessels. *J. Biomech. Eng.* 102:110–118, 1980.

10. Chen, M. M., and K. R. Holmes. Microvascular contributions in tissue heat transfer. *Ann. NY Acad. Sci.* 335:137–150, 1980.

11. Crezee, J., and J. J. W. Lagendijk. Experimental verification of bioheat transfer theories: measurement of temperature profiles around large artificial vessels in perfused tissue. *Phys. Med. Biol.* 37:905–923, 1990.

12. Crezee, J., J. Mooibroek, C. K. Bos, and J. J. W. Lagendijk. Interstitial heating: experiments in artificially perfused bovine tongues. *Phys. Med. Biol.* 36:823–833, 1991.

13. DiFelice, R. F., Jr., and H. H. Bau. Conductive heat trans-

$$A_{22} = Pe\left(-\frac{11}{96}\rho_{vr}^2\bar{u} + \frac{K'\pi\rho_{vr}^2 u}{2}\overline{W}_{v-v}\right)$$

$$A_{23} = \pi\overline{W}_{a-v} + \pi\rho_{vr}^2\overline{W}_{v-v} - \left(\frac{\eta_v^2}{2} + I_1\eta_v + I_2\right) - \frac{\rho_{vr}^2}{4}$$

$$A_{31} = \frac{PeK'\pi}{2}\overline{W}_{a-t}$$

$$A_{32} = \frac{PeK'\pi\rho_{vr}^2 u}{2}\overline{W}_{v-t}$$

$$A_{33} = \pi\overline{W}_{a-t} + \pi\rho_{vr}^2\overline{W}_{v-t} + \left\{-2D\left[\frac{H_1^3 + H_2^3}{6}\right.\right.$$
$$+ \frac{I_1(H_1^2 - H_2^2)}{2} + I_2(H_1 + H_2)\right] + \pi\left(\frac{\eta_a^2}{2}\right.$$
$$+ I_1\eta_a + I_2\right) + \frac{\pi}{8} + \rho_{vr}^2\pi\left(\frac{\eta_v^2}{2} + I_1\eta_v + I_2\right)$$
$$\left.+ \frac{\rho_{vr}^4\pi}{8}\right\}/[2D(H_1 + H_2) - \pi - \pi\rho_{vr}^2]$$

where

$$\overline{W}_{a-a} = \frac{1}{2\pi}\int_{-\pi}^{\pi} W(x,y{:}\xi_a,\eta_a)|_{\rho_a=1}d\phi_a$$

$$\overline{W}_{v-a} = \frac{1}{2\pi}\int_{-\pi}^{\pi} W(x,y{:}\xi_v,\eta_v)|_{\rho_a=1}d\phi_a$$

$$\overline{W}_{a-v} = \frac{1}{2\pi}\int_{-\pi}^{\pi} W(x,y{:}\xi_a,\eta_a)|_{\rho_v=\rho_{vr}}d\phi_v$$

$$\overline{W}_{v-v} = \frac{1}{2\pi}\int_{-\pi}^{\pi} W(x,y{:}\xi_v,\eta_v)|_{\rho_v=\rho_{vr}}d\phi_v$$

$$\overline{W}_{a-t} =$$

$$\frac{1}{[2D(H_1 + H_2) - \pi - \pi\rho_{vr}^2]}\iint\limits_{\text{tissue region}} W(x,y{:}\xi_a,\eta_a)d\Omega$$

$$\overline{W}_{v-t} =$$

$$\frac{1}{[2D(H_1 + H_2) - \pi - \pi\rho_{vr}^2]}\iint\limits_{\text{tissue region}} W(x,y{:}\xi_v,\eta_v)d\Omega$$

NOMENCLATURE

Bi	=	Biot number, $h\rho_{ar}^*/k_t$
C_f	=	specific heat of blood
D	=	half width of tissue
h	=	thermal convection coefficient
H	=	total thickness of tissue
k	=	thermal conductivity
K'	=	ratio of conductivities of vessel to tissue
l	=	vessel center to center spacing
L	=	equilibration length
Pe	=	Peclet number of the blood vessel
T	=	temperature
u	=	average blood flow velocity
$\bar{u}$	=	ratio of u_v to u_a
W	=	Green's function
x, y, z	=	Cartesian coordinates in Fig. 2
Γ	=	boundary
γ	=	density
θ	=	dimensionless temperature
θ_{a0}	=	dimensionless artery bulk temperature at $z = 0$
ξ, η	=	Cartesian coordinate
σ	=	conduction shape factor
ρ	=	radial coordinate
ρ_{vr}	=	dimensionless radius of the vein
a	=	artery
b	=	bulk
f	=	fluid in vessels
g	=	glass
s	=	source
t	=	tissue
v	=	vein
$1,2$	=	upper and lower surfaces